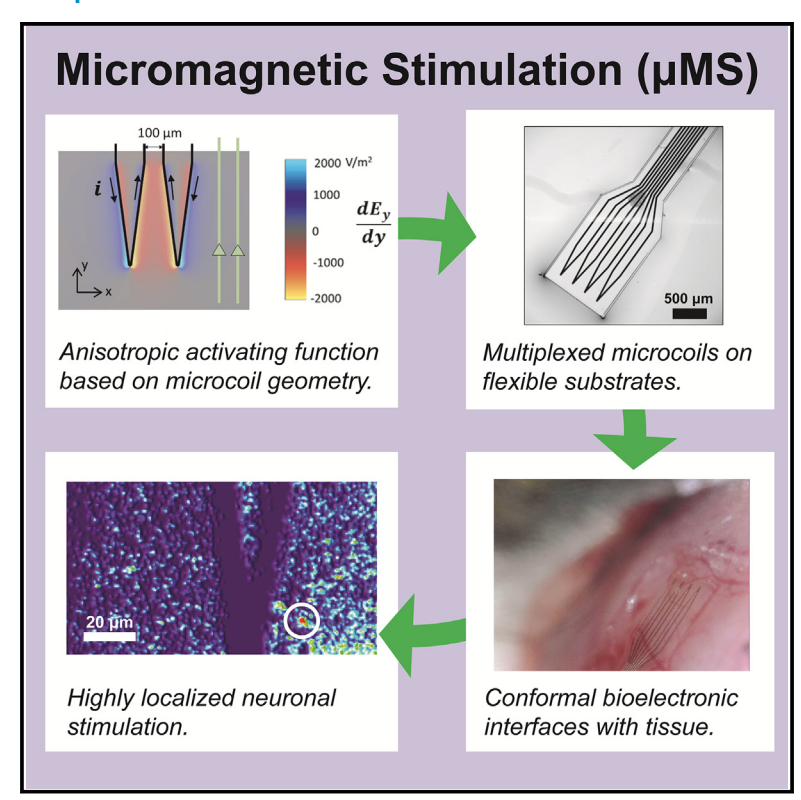
Device

Transparent and conformal microcoil arrays for spatially selective neuronal activation

Graphical abstract



Authors

Vineeth Raghuram, Aditya D. Datye, Shelley I. Fried, Brian P. Timko

Correspondence

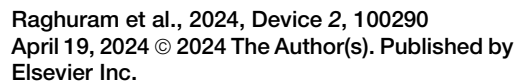
brian.timko@tufts.edu

In brief

We demonstrate a flexible, transparent, and conformal microcoil array that can activate neurons by micromagnetic stimulation. The shape and magnitude of the stimulus (activating function) can be controlled through the geometry and spacing of the microcoils. These devices achieved activation at the single-neuron level in *ex vivo* brain cortex and retina slices.

Highlights

- Micromagnetic stimulation enables neuronal activation with high spatial resolution
- Polymer-embedded coils eliminate metal-tissue interfaces improving biocompatibility
- The shape of the activating function is related to the geometry of the microcoil
- Multiplexed microcoils could enable high-acuity neural interfaces





Device



Article

Transparent and conformal microcoil arrays for spatially selective neuronal activation

Vineeth Raghuram, 1,2,3 Aditya D. Datye, 3 Shelley I. Fried, 1,2,3 and Brian P. Timko 1,4,*

¹Department of Biomedical Engineering, Tufts University, Medford, MA 02155, USA

*Correspondence: brian.timko@tufts.edu https://doi.org/10.1016/j.device.2024.100290

THE BIGGER PICTURE Neural stimulation devices could achieve many clinical functions, from mitigating neurodegenerative disorders to providing visual or tactile cues from prosthetics. Conventional devices include metallic electrodes that can cause cell damage from mechanical mismatches and prolonged electrical stimulus currents. Here, we report magnetic stimulation devices that could address these issues. They were composed of metallic microcoils embedded within bioinert polymer films. Magnetic fields pass through polymers, and so we avoided direct metal-cell interfaces. The small radius of our coils allowed us to achieve neural activation at the single- or few-neuron level. We also showed using models that the shape of the activation region could be tuned via the coil shape, potentially allowing for specific activation of aligned axons. Our studies open avenues for high-acuity bioelectronic stimulation in regions such as the retina or cortex where functions are encoded at the single-neuron level.

SUMMARY

Micromagnetic stimulation (μ MS) using small, implantable microcoils is a promising method for achieving neuronal activation with high spatial resolution and low toxicity. Herein, we report a microcoil array for localized activation of cortical neurons and retinal ganglion cells. We developed a computational model to relate the electric field gradient (activating function) to the geometry and arrangement of microcoils and selected a design that produced an anisotropic region of activation <50 μ m wide. The device comprised an SU-8/Cu/SU-8 tri-layer structure that was flexible, transparent, and conformal and featured four individually addressable microcoils. Interfaced with cortex or retina explants from GCaMP6-expressing mice, we observed that individual neurons localized within 40 μ m of a microcoil tip could be activated repeatedly and in a dose (power)-dependent fashion. These results demonstrate the potential of μ MS devices for brain-machine interfaces and could enable routes toward bioelectronic therapies including prosthetic vision devices.

INTRODUCTION

Implantable devices that achieve localized neuronal activation hold great potential in bioelectronic medicine, with applications such as treating neurological or mood disorders as well as restoring vision¹ or other sensory deficits.² Stimulation is typically achieved with multi-electrode arrays (MEAs), including Michigan- and Utah-style arrays, which are fabricated on rigid substrates and have been demonstrated intracortically. Compared with noninvasive stimulation techniques such as transcutaneous electrical nerve stimulation (TENS), these implantable devices can better confine activation, e.g., tens to hundreds of microns around the electrode site for implants vs. hundreds of microns or millimeters for TENS. More recently,

MEAs have been demonstrated on soft, stretchable, and conformal substrates. Such an approach enables all electrodes within the array to be in close proximity to complex 3D neuronal structures, e.g., the innermost surface of the retina,³ or embedded within engineered tissues, which may serve a role in disease modeling and regenerative medicine.^{4,5}

Conventional stimulation devices are composed of metallic electrodes that activate neurons through capacitive currents. While widely explored, this paradigm has several key drawbacks. First, the metallic electrodes present a large mechanical mismatch with brain tissue (Young's modulus E > 10 GPa for gold vs. 1 kPa for brain). This mismatch causes inflammation and oxidative stress at chronic time points⁶ as well as glial scarring, which ultimately limits the lifetime of the device. Second,



²Boston Veterans Affairs Healthcare System, Boston, MA 02130, USA

³Department of Neurosurgery, Massachusetts General Hospital, Harvard Medical School, Boston, MA 02114, USA

⁴Lead contact





prolonged currents themselves can also cause neuronal damage, with some stimulation regimes causing significant loss within 60 μm of the electrode after 30 days stimulation. Finally, these devices generate fields whose size and shape cannot be readily controlled, especially in inhomogeneous or anisotropic tissues, which cause irregular distribution of the electric field.8 While some studies have reported differences in activation thresholds that can be exploited to selectively activate certain neuronal sub-populations, 9-11 tissue-independent control over the shape of the field to activate neurons in a certain orientation would enable further selectivity. Taken together, these limitations present significant roadblocks toward the widespread adoption of commercial implants. 12,13

Microcoils that magnetically activate neurons could offer significant advantages over conventional metallic devices. Since magnetic fields readily permeate both tissues and biomaterials, microcoils could provide for much more reproducible activation in inhomogeneous tissues. 14,15 They could also be completely encapsulated in one or more biopolymer layers to avoid direct neuron/metal interactions. These coatings could include mechanically distinct interlayers, which were recently used to achieve bioelectronics with tissue-level moduli and minimal foreign-body responses, 16 or a bioactive layer to further enhance tissue integration.¹⁷ Chronic magnetic stimulation has also been shown to be minimally toxic to neurons. 8 Furthermore, magnetic coils generate localized, spatially asymmetric electric field gradients whose shape can be tuned through the geometry of the microcoil. These asymmetric fields are thought to enable selective targeting of specific neuronal sub-populations; for example, vertically oriented pyramidal neurons while avoiding horizontally aligned passing axon fibers. 18 Such functionality allows for more focal confinement of activation and thus could allow for the restoration of high acuity vision or enable activation in specific regions of the somatosensory cortex, e.g., to enhance feedback as part of a brain-machine interface system.

Previous studies have reported single-microcoil devices that could generate small, focal regions of activation 19 and have explored the effects of varying coil shape and design on both the spatial selectivity and strength of activation.²⁰ While devices that consist of a single microcoil may be useful in targeting one isolated region of the cortex, the ability to focally activate multiple cortical columns, or specific cortical layers, either in synchrony or in temporally modulated intervals (interleaved), would improve the translational value for clinical applications where the creation of multiple regions of neural activity is the goal.

In this study, we report a flexible, transparent, and conformal bioelectronic device that includes an array of four micromagnetic stimulation (µMS) elements. The components are composed of copper coils and encapsulated within SU-8, a photo-crosslinkable, bioinert material that has been demonstrated in chronic bioelectronic recording studies. 21,22 We develop a computational model to explore the relationship between the shape of the microcoil and resulting activating function. We then demonstrate localized activation in ex vivo tissue slices from the retina and cortex, both of which are associated with vision and are active areas of study for prosthetic devices that address blindness. Our technology represents a general platform that could be scaled to multiplexed arrays, broadened to incorporate other

bioelectronics such as recording elements, 21-26 and extended to other substrate geometries to enable, for example, injectable and minimally invasive devices.27-29

RESULTS

Computational model for coil design

We started by developing a computational model³⁰ (see experimental procedures) to explore the interaction between the electric fields induced by two adjacent coils (Figure 1). Such interactions have not been well studied and so we set out to (1) explore the relationship between coil spacing and field strength with the goal of determining an appropriate inter-coil spacing for the array and (2) examine the influence of coil shape on the potential interactions with neighboring coils. Figure 1A shows three representative tip designs: rectangular, U-shaped (radius = 75 μm), and V-shaped ($\angle = 15^{\circ}$). Similar to previous studies, ^{19,20,31} the region surrounding the arrays was modeled as a homogeneous, isotropic medium with the properties of gray matter. To isolate the effect of coil geometry, the distance between the vertical leads of the coils in each array was fixed at 100 µm and the rate of change of current through the coils was maintained at $di/dt = 1 \text{ A/}\mu\text{s}$.

Computational studies³²⁻³⁴ have shown that the strength of the gradient of the electric field (the activating function³²) arising along the length of a targeted axon is a good predictor of the effectiveness of a given set of µMS conditions. Because the axons of cortical pyramidal neurons are generally oriented in the same direction (two representative cells/axons are depicted), we started by determining the spatial gradient of the induced electric field along the length of these axons $\left(\frac{dE_y}{dy}\right)$. Gradients were calculated along a plane 10 μm below the surface of the array and are shown in the colormaps of Figure 1A. The maximum gradient levels in the maps were fixed at ±2,000 V/m² to facilitate comparisons across the three coil geometries; saturated yellow and blue regions correspond to negative (<-2,000 V/m²) and positive (>+2,000 V/m²) gradients, respectively. Since the current waveforms i(t) used in our studies have symmetric rising and falling phases, the positive and negative phases of the activating function are equivalent.

When the coil shape was rectangular (Figure 1A, left), gradients were strongest at the two right-angle bends and decreased radially with distance from the corner, thereby resulting in circular-shaped regions. The polarity of the gradient was dependent on the direction of flow of the current in the vertical portions of the microcoil (black arrows) and thus one gradient was positive and the other negative. Narrowing the width of the coil (the space between its ascending and descending vertical portions brought the opposing field gradients close to each other and resulted in reductions of the peak magnitude for each (not shown). However, because the electric current flowed in opposite directions for the two adjacent coils, the polarity of the induced field gradients was the same in the region between coils and thus there was constructive interference, and the combined field was broader and stronger. This is the same principle used for figure-of-eight coils in transcranial magnetic stimulation (TMS). 35,36 The width of the region for which the gradient magnitude $|dE_{\nu}/dy|$ exceeded 2,000 V/m² was larger than the 100-µm





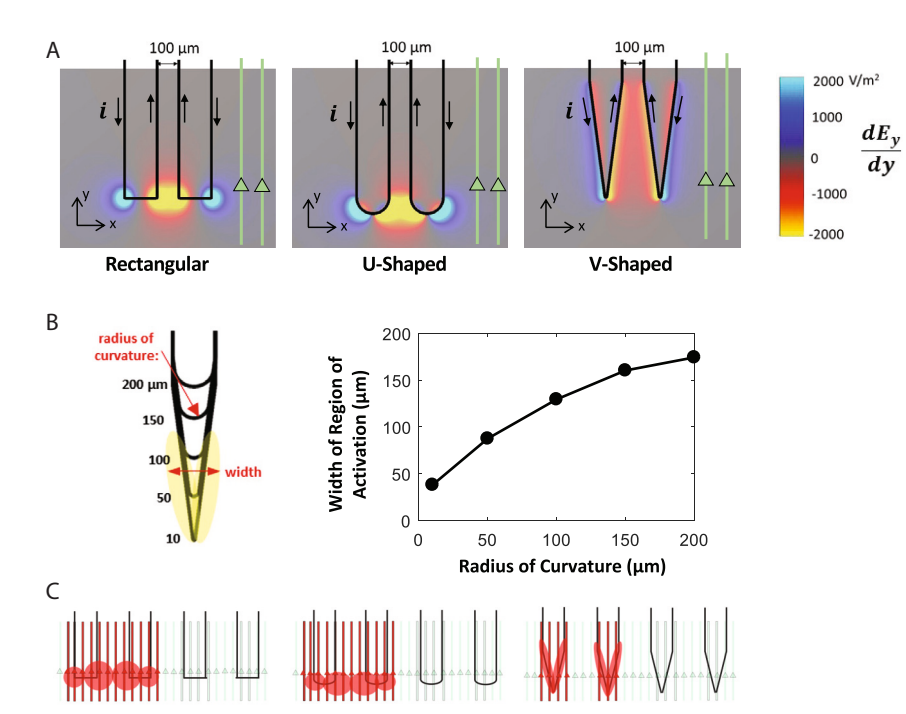


Figure 1. Computational modeling of microcoil array geometries and experimental schematic

(A) Heatmaps depicting the induced electric field gradient produced by rectangular, U- and V-shaped geometries. Gradients are calculated on a plane that is 10 μm below the bottom edge of the array and with di/dt = 1 A/μs. Black arrows depict the direction of current through the coils. Green structures represent aligned neurons/axons.

(B) Left: schematic illustration of a microcoil with a gradually increasing radius of curvature at its tip. Right: relationship between bend radius of the tip and width of the region of activation field strength | $dE_{v}/dy| > 2,000 \text{ V/m}^{2}$

(C) Schematic illustration of pyramidal neuron axons (light green) interfaced with devices and corresponding activation regions (red; adapted from the yellow regions shown in (A). Axons passing through regions of stronger gradient are more likely to be activated (red); therefore, the model predicts that V-shaped devices will offer better spatial resolution.

separation between coils. A qualitatively similar region of activation was produced when the bends in the coil tips were U-shaped (Figure 1A, middle), along with a similar overlap in the central region that both strengthened and broadened it. When the coils were V-shaped (Figure 1A, right), the regions of peak gradient were narrower, in part because the close proximity of the ascending and descending branches at the tip resulted in overlap of the positive and negative regions of field gradient. As a result, the regions of peak gradient were narrowly confined to the tip region of each coil and there was little overlap. Thus, even though the sharper bend associated with V-shaped coils produces a stronger local field, the increased separation between adjacent tips reduces the potential for overlap. Taken together, these results suggest that the use of V-shaped coils may be more effective in creating multiple, distinct regions of neural activation. In contrast, the expansive regions and overlap produced by the rectangular and U-shaped designs might result in reduced channel independence.

The relationship between coil geometry and the resulting region of field gradient was further explored by systematically varying the radius of curvature of the coil bend at the tip, which resulted in a gradual transition from a V- to U-shaped design (Figure 1B). We again calculated the width of the region of activation where $|dE_v/dy| > 2,000 \text{ V/m}^2$. Consistent with the results of Figure 1A, a smaller bend radius was associated with a narrower region of peak gradient. This pattern is analogous to the relationship between the radii of coils utilized in TMS and their induced fields; TMS coils with smaller dimensions generally produce electric fields with a smaller tangential spread.³⁷ Because our goal was to minimize the overlap between the adjacent coils, while maintaining channel independence (Figure 1C), we chose to proceed with V-shaped coil tips for subsequent physiological experiments.

Fabrication, assembly, and testing of microcoil arrays

We designed and fabricated an array with four adjacent microcoils, with the tips spaced 250 μm apart (Figures 2A and 2B). This distance was chosen to approximate the distance between adjacent cortical columns.³⁸ The device consisted of Cu coils and interconnects encapsulated by two layers of SU-8, which functioned both as flexible support substrate and passivation layer. A series of eight copper pads, with each set of two adjacent pads corresponding to the signal and ground elements for an individual coil, allowed the four coils to be individually addressed. A distance of 3.5 cm between the rectangular lavers of interconnects and the microcoils allowed for facile placement of the functional portion of the coil onto the microscope stage as well as sufficient distance between the base of the device and the chamber slide on which the tissue slice would be placed. Given that the width of a typical adult mouse cortical slice explant is around 4.5 mm and the total length between the edges of the substrate is about 1.3 mm, the multicoil array would occupy only about 30% of the tissue width and could be easily rotated to adapt to different slice orientations. Since a typical pyramidal neuron has a soma diameter of around 20-25 μm, the distance between the coils is suitable to visualize about 10 cells. Tissue could be visualized through the device via optical microscopy in both fluorescence and bright-field mode (Figure 2C), demonstrating that our system would be suitable for simultaneous calcium imaging studies.

To ensure that the fabricated coils would achieve µMS as intended, i.e., generally consistent with the model predictions, we first characterized the electrical integrity of each coil. Coils were submerged in a bath containing PBS solution and the integrity of the SU-8 insulating layer was assessed by measuring the resistance (DC impedance) between a lead connected to the coil trace and a lead inserted into the bath but adjacent to the array.





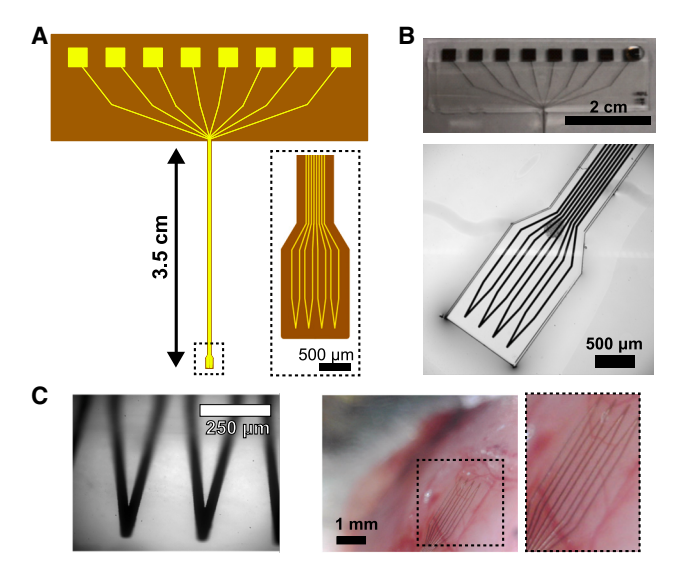


Figure 2. Fabrication and assembly of flexible microcoil devices (A) Schematic of multicoil array. Each pair of square pads addresses one coil. Inset: expanded region of stimulation region with four microcoils. (B) Photographs of (top) interconnect and (bottom) simulation regions. (C) Microcoil array interfaced with cortical tissue in (left) fluorescence and (right) bright-field mode. Inset: expansion of device and underlying tissue.

Resistance levels were typically above 200 M Ω and often exceeded 1 G Ω , implying few defects in the SU-8 layer, which was necessary to minimize the possibility of direct electrical activation of neurons by the coil. Next, the integrity of each copper trace was evaluated by measuring the resistance between the input and output leads. These measurements were typically <60 Ω , indicating good integrity of the copper trace.

Validation of microcoils for µMS

We next sought to confirm that uMS stimulation could achieve localized electric field gradients. Stimulus waveforms were generated by a function generator and amplified (see experimental procedures). For these validation studies we delivered a burst of 10 half-sinusoidal pulses with amplitudes ranging from 0 to 1,500 mV; the duration of each half sinusoid was 1 ms and there was a 4-ms interval between the offset of one waveform and the onset of the next. A glass patch pipette was positioned 5 μm above the plane of the SU-8 to measure the response in the bath resulting from the flow of current through the coil (Figures 3A and 3B; see experimental procedures). Voltage-clamp recordings from the pipette provided a qualitative assessment of the induced electric field. The responses consisted of a series of biphasic waveforms with positive and negative phases corresponding to the rising and falling elements of the input pulse (Figure 3C), as reported previously for both bent wire and fabricated coils. 18 Consistent with theory, the amplitude of the response was linearly correlated to the amplitude of the stimulus current (Figure 3D).

Selective activation of central nervous system neurons

To evaluate the efficacy of μMS with our microcoil array, we performed a series of physiological experiments using brain slices ob-

tained from the visual cortex of Thy-1 GCaMP6f-expressing mice. 18-20 In these animals, a genetically encoded fluorescent calcium indicator labels several neuronal populations within the central nervous system, including pyramidal neurons in the cortex. The fluorescence level of these neurons is positively correlated to the extent of neuronal activation, enabling responses from multiple neurons to be studied simultaneously. 18-20 The microcoil array was overlaid on the surface of the brain slice (ca. 300 μ m thickness) so that the response of layer 5 pyramidal neurons to magnetic stimulation could be visualized (Figure 4A). We delivered a series of stimuli, with each burst consisting of 20 half-sinusoidal pulses with 1 ms duration (corresponding to 500 Hz), 4 ms interpulse interval, and 500 ms interval between bursts (Figure 4Ai). These parameters were similar to those used in previous in vitro and in vivo microcoil studies. 20,39 In these preliminary experiments, we used an arbitrarily large stimulus amplitude, 200 mA, to elicit calcium responses in response to nine consecutive bursts (Figures 4Aii and 4Aiii). For the experiment shown in Figure 4Aii (right), seven or eight cells were consistently activated by the stimuli. Most were relatively close to the soma, although some were as far as 80 µm away. Note also that, although some neuropil was activated, the strength and extent of activation was much less than that for electric stimulation (Figure 4C, below).

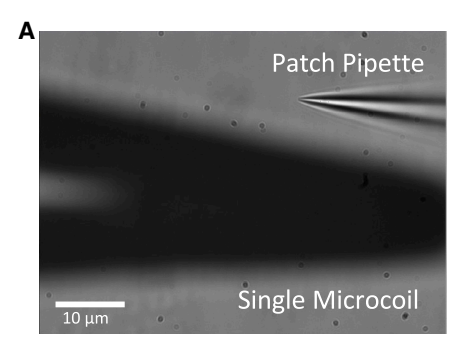
To explore the generality of our µMS approach we also stimulated retinal ganglion cells (RGCs) within a mouse retina explant (Figure 4B). Here, stimulus bursts consisted of 100 triangular pulses with 0.2 ms duration, 5 ms interpulse interval, and 1 s interval between bursts (Figure 4Bi). For these experiments we chose a pulse amplitude of 100 mA, which reliably stimulated RGCs in response to each of six consecutive bursts (Figures 4Bii and 4Biii). Similar to the case of cortex, we observed stimulation of three to four RGCs in the vicinity of the tip.

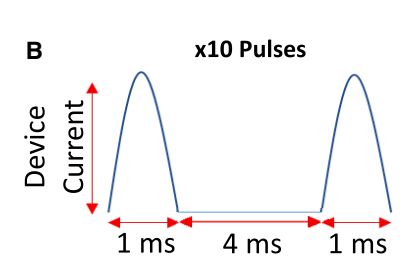
We compared the responses generated by μMS to those generated in response to electric stimulation from microelectrodes by repeating our experiments in the cortical slice using a single 10-kΩ Ptlr microelectrode (Figure 4C). Stimuli consisted of 20 square wave pulses with 0.2 ms duration and 9.6 ms interpulse interval. 19,20 The amplitude was increased until responses were elicited; in this case we used 70 µA (Figure 4Ci). The responses observed (Figures 4Cii and 4Ciii) were significantly stronger and more extensive than that from microcoils and included greater activation of neuropil and somata, e.g., moderate levels of activation were observed in Figure 4Cii (right), well beyond 100 μm. Future studies will be necessary to investigate why the activation patterns for electric vs. magnetic stimulation were so different but we believe some of the difference arises from differences in fields induced by electrodes vs. coils: the spatially symmetric fields arising from microelectrodes result in field gradients that are similar in all directions and thus activate all nearby neurons and neuronal processes, regardless of orientation. In contrast, the spatially asymmetric fields arising from coils are only effective for those neurons or neuronal processes aligned in a specific orientation.

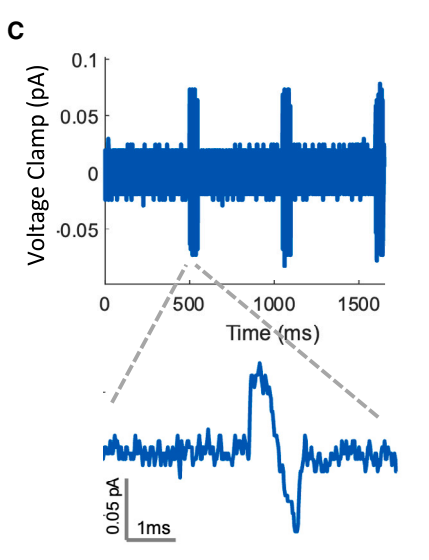
To further evaluate the efficacy of our microcoils, we studied the relationship between the amplitude of μ MS and the fluorescence change of cortical neurons (Figure 5A). Instead of simply trying to elicit responses as in Figure 4, the amplitudes of individual waveforms were systematically varied to establish the minimum level at which a calcium response was produced within

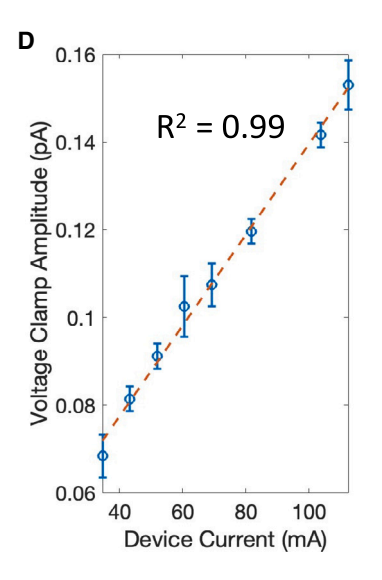
Device











individual cell bodies. Figure 5A is a representative example in which a single cell located 14.9 μm from the tip is activated. Dose-response curves are shown for a total of 11 cells (Figure 5B), where the shaded error bars indicate the standard deviation across repeated trials (n = 3). Following the approach utilized by a previous study, 40 we defined threshold as the stimulus amplitude required to elicit 50% of the maximum fluorescence change threshold (I_{50}) (see experimental procedures). The threshold for each cell was then plotted as a function of the distance from the soma to the tip of the coil (Figure 5C). Somewhat surprisingly, there was only a mild correlation between the distance from the coil and threshold (correlation coefficient: r = 0.22). However, given the small number of cells tested and potential confounding factors such as cell type and morphology, 9-11 and the relatively small distances evaluated here, further experimentation is needed to better assess this relationship. We note, however, that for these experiments the change in fluorescence was confined to a small region near the tip of the coil with the maximum distance at which a fluorescence change could be observed was <40 μm (Figures 5A and S1). We did not attempt to determine why multiple cells, some at distances of \sim 80 μ m, could be activated in some instances (e.g., Figure 4Aii), but note that, in all cases, activation from microcoil stimulation was much more narrowly confined than that from microelectrode stimulation (Figure 4C).

Figure 3. Electrical validation of flexible microcoil devices

- (A) Photograph of patch-clamp pipette positioned $5\;\mu\text{m}$ above one of the V-shaped microcoils in the fabricated array.
- (B) Schematic of the half-sinusoidal waveform used to test electrical integrity.
- (C) Top: voltage-clamp recording of the response to three bursts of the waveform bursts shown in
- (B). Bottom: expanded view of a single period.
- (D) Plot of the peak-to-peak amplitude of the response waveform as a function of the amplitude of the device stimulus current, n = 3: error bars represent SD.

DISCUSSION

We designed and fabricated a flexible, transparent, and conformal microcoil device array that could activate neurons by µMS. We showed that the width of the activating function was a monotonic function of the coil radius of curvature; thus by using a coil with a sharp V shape we could selectively activate neurons localized within 40 µm of the tip. This resolution represents a significant advance over conventional capacitively coupled electrodes and could be used to selectively activate individual neuronal pathways.

While the studies in this work were confined to μMS via a single device, the technology could be readily scaled up to

hundreds or thousands of channels, as has been achieved with MEAs. 41 Aside from achieving highly multiplexed, high-resolution inputs, µMS is advantageous in that the shape of the activating function can be tuned. We showed that our discrete devices generated anisotropic fields that might be used to selectively activate aligned axons. Previous studies using large TMS coils for activation of peripheral axon bundles ex vivo estimated field gradient thresholds of ~11,000 V/m².⁴² The corresponding thresholds for microcoil-based activation of the proximal axon of pyramidal neurons have not been well studied but it seems reasonable to assume that they are on the same order of magnitude. Computational models from earlier studies 19 suggest that field gradients from microcoils can exceed this level, although further studies with our microfabricated devices are

Systems that generate activating functions with reconfigurable magnitudes and shapes would allow for therapies that could be personalized to the patient and adapted over time. Devices that generate wide activating functions, when multiplexed, are likely to generate interference patterns, as we modeled for square- and U-shaped coils in Figure 1A. These patterns might be adjusted dynamically, by modulating the magnitude and phase of current passed through each device. Magnetic interference has been used to pattern continuous, complex geometries into composite polymer systems⁴³; similar techniques might be





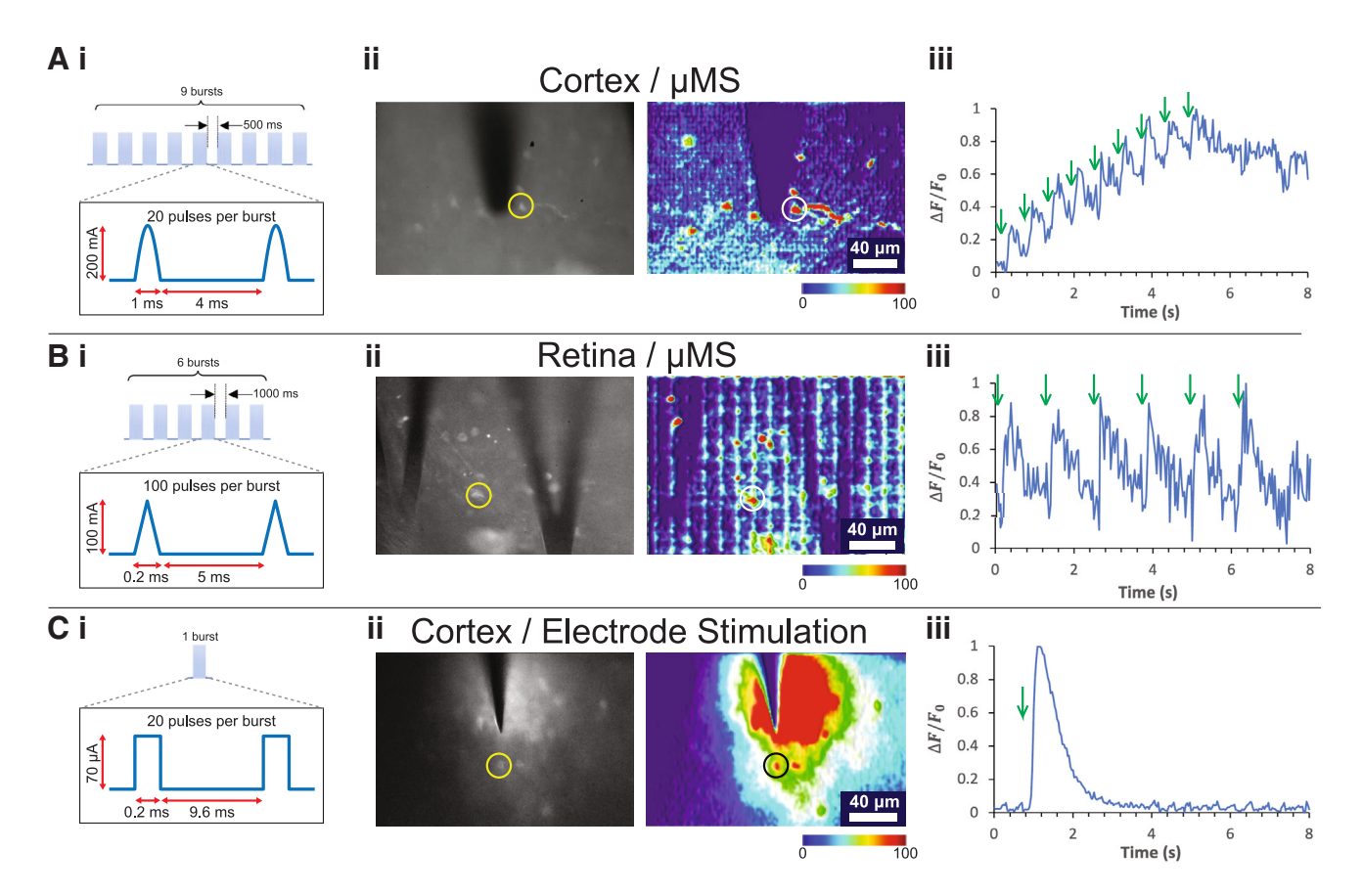


Figure 4. Stimulation and calcium fluorescence recording with ex vivo cortex and retina slices

- (A) Cortex slice interfaced with microcoil stimulation device.
- (B) Retina slice interfaced with microcoil stimulation device.
- (C) Cortex slice interfaced with 10-k Ω Ptlr microelectrode.

Sub-panels show (i) schematic of stimulus pulse bursts. Note that the x axis is not to scale to highlight the shape of the pulse. (ii) Left: fluorescence image. Right: heatmap of stimulated tissues. Both images represent peak fluorescence. (iii) Plot of fluorescence vs. time corresponding to the individual neurons indicated by circles in (ii). Green arrows indicate the onset of each waveform burst.

applied to μMS to encode information at smaller pitch than the electrodes themselves, to further increase the resolution of the technique. Alternatively, future microcoils with dynamically tunable shapes might be achieved by incorporating shape-shiftable biomaterials⁴⁴ or DNA origami, 45,46 both of which have enabled reconfigurable 3D structures on nano- to micro-length scales. Analogous approaches have already been applied on the macroscale to achieve reconfigurable electromagnetic communications devices such as antennas. 47

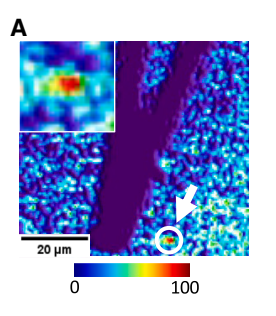
Regardless of the shape of the activating function, it will be necessary to understand the probability of neural activation for each neuron at a given distance from the electrode. Our data shown in Figure 5B show a mild correlation between the distance from the coil and the threshold for neuronal activation (r = 0.22). This variability is likely accounted for by heterogeneities in stimulation thresholds across different neurons. Previous experimental and modeling studies in rabbit RGCs found that the region of highest sensitivity (lowest threshold) for electric stimulation was along the proximal axon, about 30 µm from the soma and corresponding to a region of densely packed sodium

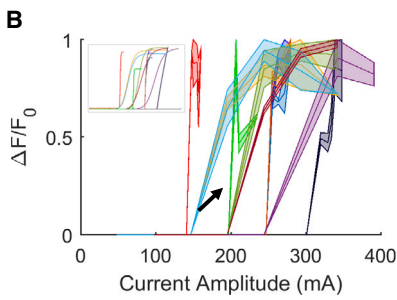
channels. This region is commonly referred to as the axon initial segment (AIS). An analogous ex vivo study in brain slices showed that the AIS also had the highest sensitivity to magnetic stimulation in layer 5 pyramidal neurons from both V1 and M1.¹⁸ The length of the AIS as well as its distance from the soma can vary considerably for different pyramidal neurons.⁴⁸ Longer AISs have lower thresholds and, thus, the combination of variable distance to the AIS as well as variable sensitivity across AISs can both contribute to variations in thresholds. We believe that these factors account for some of the sensitivity differences we observed. Furthermore, properties can vary significantly across different neuronal cell types and can contribute to variability as well.

Achieving stable interfaces between devices and tissues has been a major challenge in the bioelectronics field. Our demonstration that SU-8-encapsulated devices can achieve µMS opens avenues for high-resolution bioelectronic stimulation with minimal chronic inflammation. While SU-8 itself is much stiffer than neural tissue, it can be achieved as thin, mesh-like structures that are highly compliant because of their nonlinear









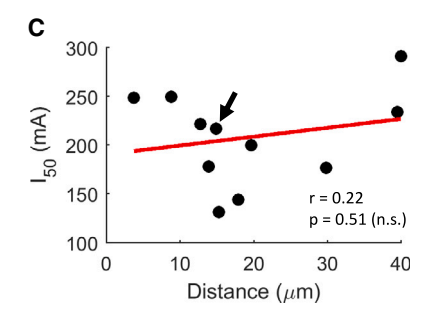


Figure 5. Cortical neurons are sensitive to stimulus amplitude

(A) Heatmap showing a single stimulated neuron (white circle and arrow) located 14.9 µm away from the device tip. Inset: detail of the stimulated neuron. (B) Dose-response curves relating fluorescence change of identified cortical neurons to amplitude of magnetic stimulation current. Each color corresponds to a different cell (11 in total, 7 slices). Shaded error bars indicate the SD across repeated trials (n = 3). Inset: sigmoid fits for each normalized dose-response curve. (C) Relationship between the distance from soma to coil tip and magnetic stimulation threshold, defined as the current required to elicit 50% of the maximum fluorescence change as shown in (B). Linear regression (red) and analysis are shown. The black arrows in (B) and (C) highlight data corresponding to the neuron shown in (A). See also Figure S1.

mechanical properties. Mesh-like bioelectronics composed of SU-8 and metallic MEA recording elements have been implanted into the retina²¹ and somatosensory cortex⁴⁹ of live mice, providing multiplexed readouts of single-unit (single-neuron) activity after processing. The cortex implants⁴⁹ were stable for at least 8 months: they provided readouts from the same neurons with little degradation of signal quality and caused minimal inflammation. Since these bioelectronics contained both devices and interconnects, it stands to reason that our µMS devices might be constructed with similar architectures to also achieve long-term interfaces with the same sets of neurons.

The µMS system reported here represents a platform technology that could interface with a wide variety of cell types, in different configurations. Aside from tuning the coil and substrate, we note several future directions. Conventional stimulation electrodes, in addition to being rigid, have a lower size limit since capacitive currents scale with surface area. Since the magnitude of the activating function is dependent on the coil radius, rather than device size, far smaller stimulation elements are conceivable. To avoid invasive surgeries, these ultrasmall microcoils might be loaded onto a catheter or other carrier and delivered to the desired location through blood vessels, as was recently demonstrated with injectable bioelectronic recording devices that were implanted into arteries overlaying the cortex and olfactory bulb.^{27,28} Biochemically functionalized µMS coils could be designed to associate with specific cellular sub-types, 50 opening further avenues for selective neuronal stimulation. Finally, μMS opens avenues for bioprobes that incorporate both simulation and recording functionalities, since the localized stimulating functions would be less likely to interfere with recordings. Such systems would enable closed-loop functionalities, which have been proposed for a wide variety of neuromodulation functions.

EXPERIMENTAL PROCEDURES

Resource availability Lead contact

Further information and requests for resources should be directed to and will be fulfilled by the lead contact, Brian P. Timko (brian.timko@tufts.edu).

Materials availability

This study did not generate new unique reagents.

Data and code availability

The authors declare that all data supporting the findings of this study are available within the paper and its supplemental information. Additional information can be requested from the lead contact.

Modeling

We developed a computational model to characterize the induced electric fields arising from the flow of electric current in an array of microcoils consisting of different coil geometries (rectangular, U-shaped, and V-shaped). We utilized a charge-based boundary element fast multipole method (BEM-FMM) toolkit to calculate the induced electric fields within the tissue. Unlike the commonly applied finite element method (FEM), BEM-FMM operates directly on tissue conductivity boundary surfaces, thus eliminating the need for volumetric meshing.³⁰ After the solution at the tissue boundaries is determined through an iterative process, the magnetic and electric fields from the flow of current through an insulated coil can be evaluated in 3D space, similar to general-purpose FEM software. An important advantage of the BEM-FMM approach is that it allows unconstrained numerical field resolution near tissue interfaces, and thus the induced fields and their spatial gradients can be calculated at a high resolution without the secondary interpolations required for volumetric FEM-based solvers. The BEM-FMM approach is also more computationally efficient compared with existing software packages. 30 The region surrounding the array (600 × 600 × 600 µm cube) was modeled as a homogeneous, isotropic medium with the properties of gray matter (electrical conductivity: $\sigma = 0.276 \text{ S/m}$), ⁵ similar to the approach used earlier to characterize the spatial extent of intracortical microcoil-based stimulation.20 After the modeling setup was defined, the BEM-FMM toolkit was utilized to calculate the electric field inside the tissue (with a spatial resolution of 1 μm) in response to an applied AC current.

In the quasistatic limit, which is commonly used when modeling electromagnetic fields in biological tissues and is considered valid for frequencies up to \sim 10 kHz, 52 the total induced electric field is given by:

$$\boldsymbol{E} = \left(-\frac{\partial \boldsymbol{A}}{\partial t}\right) + \left(-\nabla \varphi\right)$$

where \boldsymbol{A} is the magnetic vector potential and φ represents the electric potential due to surface charge redistribution at tissue conductivity boundaries.⁵³ The secondary field $(-\nabla \varphi)$ can be ignored if the primary field $\left(-\frac{\partial \mathbf{A}}{\partial t}\right)$ is parallel to the air-tissue boundary⁵⁴ as we have done here. The primary field was obtained by discretizing the coil into small, straight elements of current $i_i(t)$ with orientation \mathbf{s}_i and center coordinate \mathbf{p}_i . The





magnetic vector potential created by a current element at an observation point c_i is given by:

$$\mathbf{A}(\mathbf{c}_i,t) = \frac{\mu_0}{4\pi} \frac{i_j(t) \mathbf{s}_j}{|\mathbf{c}_i - \mathbf{p}_i|}$$

where μ_0 is the magnetic permeability of vacuum. ³⁰ The corresponding electric field generated by the current element is:

$$\boldsymbol{E}(\boldsymbol{c}_i,t) = -\frac{\partial \boldsymbol{A}(\boldsymbol{c}_i,t)}{\partial t} = -\frac{\mu_0}{4\pi} \frac{\partial i_j(t)}{\partial t} \frac{\boldsymbol{s}_j}{|\boldsymbol{c}_i - \boldsymbol{\rho}_j|}$$

The contributions from each element i of the coil are summed to find the total electric field distribution. All calculations were performed at an instant in time when the rate of change of current (di/dt) through the coil was 1 A/ μ s, which is a representative value that has been utilized in previous computational studies involving magnetic stimulation.⁵⁵ Simulations were performed on an Intel Core i7-6700 CPU (3.40 GHz, 32 GB RAM, 4 cores) with an average computation time of \sim 1 min for each simulated microcoil array.

Microfabrication protocol

All photoresists and developers were used as received from Kayaku Advanced Materials (Westborough, MA). (1) A 50-nm sacrificial layer of germanium (Ge) was sputtered onto silicon/silicon oxide substrates (300 nm, cat. no. 2525). (2) The bottom passivation layer of the device was composed of 10-μm-thick SU8 (SU8 2010) that was spin coated, patterned with UV photolithography (16 s at 15 mW/cm²) and developed with SU-8 developer for 1 min. (3) The metal layer was defined using a LOR20B/S1813 bi-layer stack followed by UV exposure (12 s at 15 mW/cm²), developed using CD-26, metallized with a 1- μm layer of copper deposited by thermal evaporation (LC Technology Solutions, Salisbury MA), and lifted off with Remover 1165 at room temperature. (4) The top passivation layer of the device was composed of $20-\mu m$ -thick SU8 (SU8 2025) that was spin coated and patterned with UV photolithography (21 s at 15 mW/cm²) with a develop time of 5 min. (5) Devices were lifted off by dissolving the Ge layer in deionized water at 80°C for up to 48 h. Next, the interconnect section (Figure 2B, top) was adhered onto a rigid plastic backing and wires were attached to the exposed copper pads using silver epoxy paste (CW2400, Chemtronics). The resistance of each device (including interconnects) was 40-60 Ω .

Magnetic and electric field generation

Magnetic fields were generated by delivering an alternating current through the microcoil. The voltage delivered to the input lead was generated with a stimulus generator in voltage mode (STG 4002, MultiChannel Systems) and amplified (PB 717X audio amplifier, 1000 W, Pyramid) with a gain of 5.6 V/V and a bandwidth of 70 kHz. 19 The ground lead of the microcoil was connected to the ground pin on the amplifier. The voltage at the input lead was confirmed using an oscilloscope and converted to current by dividing by the measured resistance of the microcoil. Electrode stimulation was performed with the same stimulus generator in current mode and a Ptlr electrode.²

Patch-clamp validation

The μMS fields were measured at a position of z = 5 μm above the surface of the microcoil using a glass pipette and a patch-clamp amplifier (MultiClamp 700B, Molecular Devices, San Jose, CA) operating in voltage-clamp mode with a holding potential of 0 mV. The pipette was positioned using a precision micromanipulator (MP-285, Sutter Instrument, Novato, CA). In brief, we first slowly lowered the pipette until it touched the surface of the device, as detected by a slight bend in the pipette tip and/or a dimple in the device surface. We defined this position as z=0 and then moved the tip 5 μ m in the positive z direction. To generate the stimuli we delivered a series of 9 current bursts through the microcoil, each consisting of 20 half-sinusoidal waveforms with 1 ms duration (corresponding to a 500 Hz sinusoidal frequency) and an interval of 4 ms between waveforms (200 waveforms/s). The magnitude of the μMS signal is proportional to the reported peak-to-peak amplitude of the current recording.

Brain slice experiments

We isolated brain slices prepared from 30- to 50-day-old mice expressing Thy1-GCaMP6f (strain no. 024339; The Jackson Laboratory), as described previously. 19,20 The care and use of animals followed all federal and institutional guidelines, the Institutional Animal Care and Use Committees of the Boston Veterans Affairs (VA) Healthcare System, and the Subcommittee on Research Animal Care of the Massachusetts General Hospital. The mice were deeply anesthetized with isoflurane and decapitated. The brains were removed immediately after death, and a section of the brain containing the visual cortex V1 (0.5-1 mm anterior from the lambdoid suture) was isolated on ice in a 0°C to 5°C oxygenated solution containing 1.25 mM NaH₂PO₄, 2.5 mM KCl, 25 mM NaHCO₃, 1 mM MgCl₂, 25 mM glucose, and 225 mM sucrose, equilibrated with 95% O2-5% CO2 (pH 7.4). This cold solution, with a low sodium ion and without calcium ion content, improved tissue viability. In the same medium, 300- to 400- μ m-thick coronal slices were prepared using a vibrating blade microtome (Vibratome 3000 Plus, Ted Pella) and were incubated at room temperature in an artificial cerebrospinal fluid (aCSF) solution containing 125 mM NaCl, 1.25 mM NaH₂PO₄, 2.5 mM KCl, 25 mM NaHCO₃, 1 mM MgCl₂, 2 mM CaCl₂, and 25 mM glucose, equilibrated with 95% O₂-5% CO₂ (pH 7.4). After a 2-h recovery period, slices that contained V1 were transferred and mounted, caudal side down, to a plastic recording chamber (RC-27L, Warner Instruments) with a plastic slice anchor (SHD-27LP/2, Warner Instruments). The chamber was maintained at 30° C \pm 2° C and continuously superfused (3.3 mL/min) with oxygenated aCSF solution.

Fluorescence microscopy

Brain slices were prepared and maintained as described above and were then incubated in a dark room at room temperature in aCSF solution. After a 2-h recovery period, slices that contained the primary visual cortex (V1) were transferred and mounted, caudal side down, to the plastic recording chamber (RC-27L) with a plastic slice anchor (SHD-27LP/2). Imaging was performed with a Nikon Eclipse FN1 microscope (Nikon Instruments) through a 20 x 0.5 numerical aperture objective (Nikon Fluor 20×/0.50 water immersion objective). The excitation light source (X-Cite 120Q; Excelitas Technologies) was coupled to the epifluorescent port of the microscope. Calcium fluorescence changes were captured with a sCMOS camera (USB 3.1 Gen 1; 2,048 × 2,048; 30 frames/s; PCO.Panda 4.2). Images were recorded and then processed post hoc using image analysis software (ImageJ/FIJI: National Institutes of Health). Outlines around the somas of individual pyramidal neurons were defined to create ROIs. The calcium fluorescence transients for individual neurons were calculated as $(\Delta F/F_0) = (F - F_0)/F_0$, where F_0 was the baseline fluorescence level calculated by averaging over 2 s before the onset of stimulation, and subsequently normalized to max observed fluorescence change.

Data analysis

MATLAB's "fitnlm" function was utilized to fit each dose-response curve with a four-parameter sigmoidal function defined by F'(I) = $F'_{\text{min}} + (F'_{\text{max}} - F'_{\text{min}}) / [1 + (I_{50}/I)^{\beta}]$, where $F' = (\Delta F / F_0)$ and β is the dynamic range. I50 is the current amplitude required to elicit 50% of the maximum fluorescence change; this was used as an estimate for the threshold of magnetic stimulation.

SUPPLEMENTAL INFORMATION

Supplemental information can be found online at https://doi.org/10.1016/j. device 2024 100290

ACKNOWLEDGMENTS

This research was supported by NSF CAREER 2239557 (to B.P.T.), AHA 23TPA1057212 (to B.P.T), NIH R21EB034527 (to B.P.T.), BRAIN R01-NS110575 (to S.I.F), and DOD/CDMRP VR170089 (to S.I.F).

AUTHOR CONTRIBUTIONS

Conceptualization, V.R., S.I.F., and B.P.T.; methodology, V.R., S.I.F., and B.P.T.; software, A.D.D.; investigation, A.D.D. and V.R.; resources, S.I.F. and





B.P.T.; writing - original draft, V.R. and A.D.D.; writing - review & editing, V.R., A.D.D., S.I.F., and B.P.T.; supervision, S.I.F. and B.P.T.; funding acquisition, S.I.F. and B.P.T.

DECLARATION OF INTERESTS

S.I.F. declares the following intellectual property: US Patent no. 9,993,656, "Magnetic neural stimulator and method of activation of neural tissue with same"; and Application no. 11,007,372, "Selective activation of cortex using bent micro-wires to magnetically stimulate neurons."

Received: November 27, 2023 Revised: January 12, 2024 Accepted: January 28, 2024 Published: March 5, 2024

REFERENCES

- 1. Jang, J., Kim, H., Song, Y.M., and Park, J.U. (2019). Implantation of electronic visual prosthesis for blindness restoration. Opt. Mater. Express 9, 3878-3894. https://doi.org/10.1364/Ome.9.003878.
- 2. Raspopovic, S., Valle, G., and Petrini, F.M. (2021). Sensory feedback for limb prostheses in amputees. Nat. Mater. 20, 925-939. https://doi.org/ 10.1038/s41563-021-00966-9.
- 3. Chenais, N.A.L., Airaghi Leccardi, M.J.I., and Ghezzi, D. (2021). Photovoltaic retinal prosthesis restores high-resolution responses to single-pixel stimulation in blind retinas. Commun. Mater. 2, 28. https://doi.org/10. 1038/s43246-021-00133-2.
- 4. Feiner, R., and Dvir, T. (2020). Engineering Smart Hybrid Tissues with Built-In Electronics. iScience 23, 100833. https://doi.org/10.1016/j.isci.2020. 100833
- 5. Dai, X., Hong, G., Gao, T., and Lieber, C.M. (2018). Mesh Nanoelectronics: Seamless Integration of Electronics with Tissues. Acc. Chem. Res. 51, 309-318. https://doi.org/10.1021/acs.accounts.7b00547.
- 6. Ereifej, E.S., Rial, G.M., Hermann, J.K., Smith, C.S., Meade, S.M., Rayyan, J.M., Chen, K., Feng, H., and Capadona, J.R. (2018). Implantation of Neural Probes in the Brain Elicits Oxidative Stress. Front. Bioeng. Biotechnol. 6, 9. https://doi.org/10.3389/fbioe.2018.00009.
- 7. McCreery, D., Pikov, V., and Troyk, P.R. (2010). Neuronal loss due to prolonged controlled-current stimulation with chronically implanted microelectrodes in the cat cerebral cortex. J. Neural. Eng. 7, 036005. https:// doi.org/10.1088/1741-2560/7/3/036005.
- 8. Ye, H., Hendee, J., Ruan, J., Zhirova, A., Ye, J., and Dima, M. (2022). Neuron matters: neuromodulation with electromagnetic stimulation must consider neurons as dynamic identities. J. NeuroEng. Rehabil. 19, 116. https://doi.org/10.1186/s12984-022-01094-4.
- 9. Raghuram, V., Werginz, P., Fried, S.I., and Timko, B.P. (2021). Morphological Factors that Underlie Neural Sensitivity to Stimulation in the Retina. Adv. Nanobiomed Res. 1, 2100069. https://doi.org/10.1002/ anbr.202100069.
- 10. Fried, S.I., Lasker, A.C., Desai, N.J., Eddington, D.K., and Rizzo, J.F., 3rd. (2009). Axonal sodium-channel bands shape the response to electric stimulation in retinal ganglion cells. J. Neurophysiol. 101, 1972-1987. https:// doi.org/10.1152/jn.91081.2008.
- 11. Werginz, P., Raghuram, V., and Fried, S.I. (2020). The relationship between morphological properties and thresholds to extracellular electric stimulation in RGCs. J. Neural. Eng. 17, 045015. https://doi.org/10.1088/1741-2552/abab47.
- 12. Fernández, E., Alfaro, A., and González-López, P. (2020). Toward Long-Term Communication With the Brain in the Blind by Intracortical Stimulation: Challenges and Future Prospects. Front. Neurosci. 14, 681. https:// doi.org/10.3389/fnins.2020.00681.
- 13. Lewis, P.M., Ackland, H.M., Lowery, A.J., and Rosenfeld, J.V. (2015). Restoration of vision in blind individuals using bionic devices: a review

- with a focus on cortical visual prostheses. Brain Res. 1595, 51-73. https://doi.org/10.1016/j.brainres.2014.11.020.
- 14. Williams, J.C., Hippensteel, J.A., Dilgen, J., Shain, W., and Kipke, D.R. (2007). Complex impedance spectroscopy for monitoring tissue responses to inserted neural implants. J. Neural. Eng. 4, 410-423. https:// doi.org/10.1088/1741-2560/4/4/007.
- 15. Kozai, T.D.Y., Jaquins-Gerstl, A.S., Vazquez, A.L., Michael, A.C., and Cui, X.T. (2015). Brain tissue responses to neural implants impact signal sensitivity and intervention strategies. ACS Chem. Neurosci. 6, 48-67. https:// doi.org/10.1021/cn500256e.
- 16. Li, Y., Li, N., Liu, W., Prominski, A., Kang, S., Dai, Y., Liu, Y., Hu, H., Wai, S., Dai, S., et al. (2023). Achieving tissue-level softness on stretchable electronics through a generalizable soft interlayer design. Nat. Commun. 14, 4488. https://doi.org/10.1038/s41467-023-40191-3.
- 17. Ju, J., Hu, N., Cairns, D.M., Liu, H., and Timko, B.P. (2020). Photo-crosslinkable, insulating silk fibroin for bioelectronics with enhanced cell affinity. Proc. Natl. Acad. Sci. USA 117, 15482-15489. https://doi.org/10.1073/ pnas.2003696117.
- 18. Lee, S.W., and Fried, S.I. (2017). Enhanced Control of Cortical Pyramidal Neurons With Micromagnetic Stimulation. IEEE Trans. Neural Syst. Rehabil. Eng. 25, 1375-1386. https://doi.org/10.1109/TNSRE.2016.2631446.
- 19. Lee, S.W., Fallegger, F., Casse, B.D.F., and Fried, S.I. (2016). Implantable microcoils for intracortical magnetic stimulation. Sci. Adv. 2, e1600889. https://doi.org/10.1126/sciadv.1600889.
- 20. Lee, S.W., Thyagarajan, K., and Fried, S.I. (2019). Micro-Coil Design Influences the Spatial Extent of Responses to Intracortical Magnetic Stimulation. IEEE Trans. Biomed. Eng. 66, 1680-1694. https://doi.org/10.1109/ TBME.2018.2877713.
- 21. Hong, G., Fu, T.M., Qiao, M., Viveros, R.D., Yang, X., Zhou, T., Lee, J.M., Park, H.G., Sanes, J.R., and Lieber, C.M. (2018). A method for singleneuron chronic recording from the retina in awake mice. Science 360, 1447-1451. https://doi.org/10.1126/science.aas9160.
- 22. Zhou, T., Hong, G., Fu, T.M., Yang, X., Schuhmann, T.G., Viveros, R.D., and Lieber, C.M. (2017). Syringe-injectable mesh electronics integrate seamlessly with minimal chronic immune response in the brain. Proc. Natl. Acad. Sci. USA 114, 5894-5899. https://doi.org/10.1073/pnas. 1705509114.
- 23. Kalmykov, A., Reddy, J.W., Bedoyan, E., Wang, Y., Garg, R., Rastogi, S.K., Cohen-Karni, D., Chamanzar, M., and Cohen-Karni, T. (2021). Bioelectrical interfaces with cortical spheroids in three-dimensions. J. Neural. Eng. 18, 055005. https://doi.org/10.1088/1741-2552/abf290.
- 24. Park, Y., Franz, C.K., Ryu, H., Luan, H., Cotton, K.Y., Kim, J.U., Chung, T.S., Zhao, S., Vazquez-Guardado, A., Yang, D.S., et al. (2021). Threedimensional, multifunctional neural interfaces for cortical spheroids and engineered assembloids. Sci. Adv. 7, eabf9153. https://doi.org/10.1126/
- 25. Le Floch, P., Li, Q., Lin, Z., Zhao, S., Liu, R., Tasnim, K., Jiang, H., and Liu, J. (2022). Stretchable Mesh Nanoelectronics for 3D Single-Cell Chronic Electrophysiology from Developing Brain Organoids. Adv. Mater. 34, e2106829. https://doi.org/10.1002/adma.202106829.
- 26. Yang, X., Forró, C., Li, T.L., Miura, Y., Zaluska, T.J., Tsai, C.T., Kanton, S., McQueen, J.P., Chen, X., Mollo, V., et al. (2024). Kirigami electronics for long-term electrophysiological recording of human neural organoids and assembloids. Nat. Biotechnol., 1-5. https://doi.org/10.1038/s41587-023-02081-3.
- 27. Zhang, A., Mandeville, E.T., Xu, L., Stary, C.M., Lo, E.H., and Lieber, C.M. (2023). Ultraflexible endovascular probes for brain recording through micrometer-scale vasculature. Science 381, 306-312. https://doi.org/10. 1126/science.adh3916.
- 28. Timko, B.P. (2023). Neural implants without brain surgery. Science 381, 268-269. https://doi.org/10.1126/science.adi9330.
- 29. Han, M., Chen, L., Aras, K., Liang, C., Chen, X., Zhao, H., Li, K., Faye, N.R., Sun, B., Kim, J.H., et al. (2020). Catheter-integrated soft multilayer





- electronic arrays for multiplexed sensing and actuation during cardiac surgery. Nat. Biomed. Eng. 4, 997-1009. https://doi.org/10.1038/s41551-020-00604-w.
- 30. Makarov, S.N., Wartman, W.A., Daneshzand, M., Fujimoto, K., Raij, T., and Nummenmaa, A. (2020). A software toolkit for TMS electric-field modeling with boundary element fast multipole method: an efficient MATLAB implementation. J. Neural. Eng. 17, 046023. https://doi.org/10.1088/1741-2552/ab85b3.
- 31. Bonmassar, G., Lee, S.W., Freeman, D.K., Polasek, M., Fried, S.I., and Gale, J.T. (2012). Microscopic magnetic stimulation of neural tissue. Nat. Commun. 3, 921. https://doi.org/10.1038/ncomms1914.
- 32. Rattay, F. (1986). Analysis of models for external stimulation of axons. IEEE Trans. Biomed. Eng. 33, 974-977. https://doi.org/10.1109/TBME.1986. 325670
- 33. Basser, P.J., Wijesinghe, R.S., and Roth, B.J. (1992). The activating function for magnetic stimulation derived from a three-dimensional volume conductor model. IEEE Trans. Biomed. Eng. 39, 1207-1210. https://doi. org/10.1109/10.168686.
- 34. Esselle, K.P., and Stuchly, M.A. (1992). Neural stimulation with magnetic fields: analysis of induced electric fields. IEEE Trans. Biomed. Eng. 39, 693-700. https://doi.org/10.1109/10.142644.
- 35. Ravazzani, P., Ruohonen, J., Grandori, F., and Tognola, G. (1996). Magnetic stimulation of the nervous system: induced electric field in unbounded, semi-infinite, spherical, and cylindrical media. Ann. Biomed. Eng. 24, 606-616. https://doi.org/10.1007/BF02684229.
- 36. Ruohonen, J., and Ilmoniemi, R.J. (1998). Focusing and targeting of magnetic brain stimulation using multiple coils. Med. Biol. Eng. Comput. 36, 297-301. https://doi.org/10.1007/BF02522474.
- 37. Deng, Z.D., Lisanby, S.H., and Peterchev, A.V. (2013). Electric field depthfocality tradeoff in transcranial magnetic stimulation; simulation comparison of 50 coil designs. Brain Stimul. 6, 1-13. https://doi.org/10.1016/j.brs. 2012.02.005.
- 38. Bonin, V., Histed, M.H., Yurgenson, S., and Reid, R.C. (2011). Local diversity and fine-scale organization of receptive fields in mouse visual cortex. J. Neurosci. 31, 18506-18521. https://doi.org/10.1523/JNEUROSCI. 2974-11.2011.
- 39. Ryu, S.B., Paulk, A.C., Yang, J.C., Ganji, M., Dayeh, S.A., Cash, S.S., Fried, S.I., and Lee, S.W. (2020). Spatially confined responses of mouse visual cortex to intracortical magnetic stimulation from micro-coils. J. Neural. Eng. 17, 056036. https://doi.org/10.1088/1741-2552/abbd22.
- 40. Larsch, J., Ventimiglia, D., Bargmann, C.I., and Albrecht, D.R. (2013). High-throughput imaging of neuronal activity in Caenorhabditis elegans. Proc. Natl. Acad. Sci. USA 110, E4266-E4273. https://doi.org/10.1073/ pnas.1318325110.
- 41. Chen, X., Wang, F., Fernandez, E., and Roelfsema, P.R. (2020). Shape perception via a high-channel-count neuroprosthesis in monkey visual cortex. Science 370, 1191-1196. https://doi.org/10.1126/science.
- 42. Maccabee, P.J., Amassian, V.E., Eberle, L.P., and Cracco, R.Q. (1993). Magnetic coil stimulation of straight and bent amphibian and mammalian

- peripheral nerve in vitro: locus of excitation. J. Physiol. 460, 201-219. https://doi.org/10.1113/jphysiol.1993.sp019467.
- 43. Yang, Z., Wei, J., Giżynski, K., Song, M.G., and Grzybowski, B.A. (2017). Interference-like patterns of static magnetic fields imprinted into polymer/nanoparticle composites. Nat. Commun. 8, 1564. https://doi.org/10. 1038/s41467-017-01861-1.
- 44. Jiao, Y., Zhang, Y., Feng, H., Li, H., Wang, Z., Wang, P., Wang, Y., Zheng, N., Xie, T., Ma, Y., and Feng, X. (2023). A Multifunctional Bioelectronic Device with Switchable Rigidity and Reconfigurable Shapes for Comprehensive Diagnosis. Adv. Electron. Mater. 9. https://doi.org/10.1002/aelm. 202201343.
- 45. Sarraf, N., Rodriguez, K.R., and Qian, L. (2023). Modular reconfiguration of DNA origami assemblies using tile displacement. Sci. Robot. 8, eadf1511. https://doi.org/10.1126/scirobotics.adf1511.
- 46. Kim, M., Lee, C., Jeon, K., Lee, J.Y., Kim, Y.J., Lee, J.G., Kim, H., Cho, M., and Kim. D.N. (2023). Harnessing a paper-folding mechanism for reconfigurable DNA origami. Nature 619, 78-86. https://doi.org/10.1038/s41586-023-06181-7.
- 47. Mackertich-Sengerdy, G., Campbell, S.D., and Werner, D.H. (2023). Tailored compliant mechanisms for reconfigurable electromagnetic devices. Nat. Commun. 14, 683. https://doi.org/10.1038/s41467-023-
- 48. Höfflin, F., Jack, A., Riedel, C., Mack-Bucher, J., Roos, J., Corcelli, C., Schultz, C., Wahle, P., and Engelhardt, M. (2017). Heterogeneity of the Axon Initial Segment in Interneurons and Pyramidal Cells of Rodent Visual Cortex. Front. Cell. Neurosci. 11, 332. https://doi.org/10.3389/fncel.2017. 00332.
- 49. Fu, T.M., Hong, G., Zhou, T., Schuhmann, T.G., Viveros, R.D., and Lieber, C.M. (2016). Stable long-term chronic brain mapping at the single-neuron level. Nat. Methods 13, 875-882. https://doi.org/10.1038/nmeth.3969.
- 50. Zhang, A., Zwang, T.J., and Lieber, C.M. (2023). Biochemically functionalized probes for cell-type-specific targeting and recording in the brain. Sci. Adv. 9, eadk1050. https://doi.org/10.1126/sciadv.adk1050.
- 51. Wagner, T., Fregni, F., Eden, U., Ramos-Estebanez, C., Grodzinsky, A., Zahn, M., and Pascual-Leone, A. (2006). Transcranial magnetic stimulation and stroke: a computer-based human model study. Neuroimage 30, 857-870. https://doi.org/10.1016/j.neuroimage.2005.04.046.
- 52. Janssen, A.M., Oostendorp, T.F., and Stegeman, D.F. (2015). The coil orientation dependency of the electric field induced by TMS for M1 and other brain areas. J. NeuroEng. Rehabil. 12, 47. https://doi.org/10.1186/ s12984-015-0036-2.
- 53. Miranda, P.C., Hallett, M., and Basser, P.J. (2003). The electric field induced in the brain by magnetic stimulation: a 3-D finite-element analysis of the effect of tissue heterogeneity and anisotropy. IEEE Trans. Biomed. Eng. 50, 1074-1085. https://doi.org/10.1109/TBME.2003.816079.
- 54. Wang, B., Grill, W.M., and Peterchev, A.V. (2018), Coupling Magnetically Induced Electric Fields to Neurons: Longitudinal and Transverse Activation. Biophys. J. 115, 95–107. https://doi.org/10.1016/j.bpj.2018.06.004.
- 55. Roth, B.J., and Basser, P.J. (1990). A model of the stimulation of a nerve fiber by electromagnetic induction. IEEE Trans. Biomed. Eng. 37, 588-597. https://doi.org/10.1109/10.55662.